nature communications

Article

https://doi.org/10.1038/s41467-025-57823-5

Identification of a non-inhibitory aptameric ligand to CRL2^{ZYG11B} E3 ligase for targeted protein degradation

Received: 26 August 2024

Accepted: 5 March 2025

Published online: 13 March 2025

Check for updates

Zhihao Yang[1,11], Miao Chen[2,11], Ruixin Ge[3], Ping Zhou[3], Wei Pan[3], Jiayi Song[4], Shuwen Ma[4], Song Chen[4], Chenyu Xu[5], Mengyu Zhou[6], Wenyi Mi[6], Hua Ni[7], He Chen[8], Xue Yao[9], Xifeng Dong[10], Yan Chen[3], Jun Zhou[3,7], Chenghao Xuan[1,6] ✉, Cheng Dong[1,6] ✉, Hua Yan[4] ✉ & Songbo Xie[1,3,4] ✉

As a crucial element of proteolysis targeting chimeras (PROTACs), the choice of E3 ubiquitin ligase significantly influences degradation efficacy and selectivity. However, the available arsenal of E3 ligases for PROTAC development remains underexplored, severely limiting the scope of targeted protein degradation. In this study, we identify a non-inhibitory aptamer targeting ZYG11B, a substrate receptor of the Cullin 2-RING ligase complex, as an E3 warhead for targeted protein degradation. This aptamer-based PROTAC platform, termed ZATAC, is facilely produced through bioorthogonal chemistry or self-assembly and shows promise in eliminating several undruggable target proteins, including nucleolin (NCL), SRY-box transcription factor 2 (SOX2), and mutant p53-R175H, underscoring its universality and versatility. To specifically deliver ZATACs into cancer cells, we further develop DNA three-way junction-based ZATACs (3WJ-ZATACs) by integrating an additional aptamer that selectively recognizes the protein overexpressed on the surface of cancer cells. The 3WJ-ZATACs demonstrate in vivo tumor-specific distribution and achieve dual-target degradation, thereby suppressing tumor growth without causing noticeable toxicity. In summary, ZATACs represent a general, modular, and straightforward platform for targeted protein degradation, offering insights into the potential of other untapped E3 ligases.

Proteolysis-targeting chimeras (PROTACs) have emerged as a promising therapeutic modality over the past decades[1,2]. These heterobifunctional molecules induce proximity between an E3 ligase and a protein of interest (POI), facilitating the degradation of the POI through proteasomal pathways[3,4]. The E3 ligase plays a crucial role in PROTAC-mediated degradation. However, out of more than 600 E3 ligases encoded by the human genome, only about 2% have been effectively engaged in the design of functional PROTACs to date[1,5]. Typically, the substrate recognition components cereblon (CRBN) and von Hippel-Lindau (VHL) are the most used E3 ligases for PROTAC development[6,7]. However, preclinical studies of degraders utilizing CRBN or VHL have identified emerging resistance mechanisms, including mutations and/or downregulation of components within the ubiquitin ligase machinery[5]. Moreover, the proper pairing of the E3 ligase with the target protein is critical for ternary complex formation and consequently affects the efficacy and selectivity of degradation[1,8]. Therefore, identifying novel E3 ligase ligands is of paramount importance in advancing the field of targeted protein degradation.

Like CRBN and VHL, Zyg-11 family member B (ZYG11B) serves as a substrate receptor within the Cullin 2-RING E3 ubiquitin ligase (CRL2)

A full list of affiliations appears at the end of the paper. ✉e-mail: chenghaoxuan@tmu.edu.cn; dongcheng@tmu.edu.cn; zyyyanhua@tmu.edu.cn; songboxie@tmu.edu.cn

complex[9]. ZYG11B recognizes substrate proteins containing N-terminal glycine degrons (Gly/N-degron), which are strongly enriched during apoptosis due to caspase cleavage, thereby playing a crucial role in protein quality control and maintenance of protein homeostasis[10,11]. In addition, ZYG11B also recognizes N-terminal serine (Nt-Ser), alanine (Nt-Ala), and cysteine (Nt-Cys), thus participating in Nt-acetylation quality control[12]. Recent studies have revealed that ZYG11B is implicated in diverse activities, including SARS-CoV-2 infection, antiviral innate immune response, and chemoresistance in colorectal cancer cells[13–15]. Given the critical role of ZYG11B in substrate recognition and protein quality control, it is tempting to discover novel ligands specifically targeting this protein for PROTAC development.

Aptamers, often referred to as 'chemical antibodies', are single-stranded oligonucleotides derived through a gold-standard method known as Systematic Evolution of Ligands by Exponential Enrichment (SELEX)[16]. They offer many advantages over traditional antibodies, including ease of chemical synthesis and modification, high tissue penetration, negligible immunogenicity, and capabilities in structural switching and self-assembly[16]. Aptamers have been extensively applied in the construction of biosensors and as drug delivery carriers[17]. Over the past three years, the emergence of aptamer-based targeted protein degradation strategies[18], including aptamer–PROTAC conjugates (APCs)[19], aptamer-based PROTACs[20–22], and aptamer-LYTACs[23,24], has introduced novel approaches for targeting proteins implicated in disease pathogenesis. Despite these innovations, aptamers targeting E3 ligases have yet to be utilized in PROTAC discovery.

In this study, we identify a novel aptamer, Apt#Z6, that selectively engages $CRL2^{ZYG11B}$ without disrupting its ubiquitin ligase activity. Consequently, we develop bispecific and trispecific PROTACs based on this E3 ligase-targeted aptamer, referred to as ZYG11B aptamer-based PROTACs (ZATACs). ZATACs demonstrate robust and potent degradation capabilities against a range of proteins, including GFP-HaloTag, nucleolin (NCL), SRY-box transcription factor 2 (SOX2), and p53-R175H. Furthermore, the trispecific ZATACs enable tumor-specific uptake and dual-target degradation. Overall, ZATACs broaden the arsenal of E3 ligases and offer insights for engaging other E3 ligases, representing a pioneering advancement in the field of targeted protein degradation.

Results

Identification of a non-inhibitory DNA aptamer targeting ZYG11B via SELEX

Leveraging aptamers as molecular ligands for targeted protein degradation represents a promising approach, owing to the relative ease of selection via SELEX. To broaden the repertoire of E3 ligases for PROTAC discovery, we employed magnetic bead-based SELEX to identify highly specific ligands for ZYG11B (Fig. 1a). After several rounds of selection under progressively stringent conditions (Supplementary Table 1), the retention rate significantly improved and reached saturation in the final two rounds (Fig. 1b). We subsequently analyzed the enriched aptamers from each round using next-generation sequencing. The 50 most abundant sequences were categorized into five families (Supplementary Fig. 1a), from which ten sequences were selected for validation. Isothermal titration calorimetry (ITC) assays revealed that Apt#Z6 demonstrated the highest affinity, with a *Kd* value of 4.69 ± 2.19 μM (Fig. 1c, d). The binding interaction between Apt#Z6 and ZYG11B was further confirmed through surface plasmon resonance (SPR) and microscale thermophoresis (MST) assays (Supplementary Fig. 1b, c).

To validate the specific interaction between Apt#Z6 and ZYG11B in cellular contexts, we enriched proteins associated with biotin-Apt#Z6 by streptavidin pulldown assays and found that GFP-tagged ZYG11B was captured by biotin-Apt#Z6, while competitive inhibition with untagged Apt#Z6 attenuated this binding (Fig. 1e), underscoring the specificity of the interaction. Coomassie brilliant blue staining identified an enhanced band around 80 kDa in the biotin-Apt#Z6 group compared to the beads and biotin-library control (Supplementary Fig. 1d). Subsequent analysis of the bands by mass spectrometry revealed that ZYG11B is a highly credible Apt#Z6-interacting candidate as it was exclusively enriched in biotin-Apt#Z6 whereas not detected in the biotin-library control (Supplementary Table 2). In addition, its homolog protein ZER1 was nearly undetectable in both the biotin-library and biotin-Apt#Z6 groups. Consistently, ITC assays revealed that Apt#Z6 did not bind to purified ZER1 (Supplementary Fig 1e). We next examined the colocalization of Apt#Z6 with ZYG11B in cells. In line with our streptavidin pull-down data, Cy3-labeled Apt#Z6 was found to colocalize with GFP-tagged ZYG11B in HEK293T cells (Supplementary Fig. 1f).

Specific binding without inhibitory activity is essential for an E3 ligase ligand to induce targeted protein degradation effectively. Given that $CRL2^{ZYG11B}$ selectively targets proteins with Gly/N-degrons and small N-terminal residues for degradation, we investigated whether Apt#Z6 impacts the ubiquitin ligase activity of $CRL2^{ZYG11B}$ using a ubiquitin global protein stability (GPS) reporter (Supplementary Fig. 2a). We observed that overexpression of exogenous ZYG11B led to the degradation of an N-degron-GFP fusion protein and treatment with Apt#Z6 had minimal effect on this process (Supplementary Figs. 2b, c). Immunoblotting analyses further confirmed that Apt#Z6 did not interfere with ZYG11B-mediated degradation of the N-degron-GFP fusion protein (Supplementary Fig. 2d). Consistently, Apt#Z6 did not alter the expression levels of ZYG11B protein and its substrate JAK2[11] (Supplementary Fig. 2e). These data indicate the suitability of Apt#Z6 as an E3 ligand for PROTAC applications. In addition, we assessed the serum stability of Apt#Z6 and confirmed its stability up to the 24 h (Supplementary Figs. 2f, g). Collectively, these findings underscore the potential of Apt#Z6 as a non-inhibitory ligand to the $CRL2^{ZYG11B}$ E3 ligase for targeted protein degradation.

Apt#Z6 is a well-suited candidate for targeted protein degradation

To test the feasibility of Apt#Z6 for targeted protein degradation, we conjugated it with a DBCO-modified HaloTag ligand using bioorthogonal chemistry to construct HaloPROTACs (Fig. 2a), a commonly utilized tag-targeted protein degrader system[25,26]. These Apt#Z6-based HaloPROTACs, named Halo-ZATACs, specifically target exogenous GFP-HaloTag for degradation (Fig. 2b). Compared to azide-modified Apt#Z6 (N_3-Apt#Z6), a slight mobility shift was observed in 20% native PAGE, indicating successful conjugation of Halo-ZATAC#T0 (Supplementary Fig. 3a). However, Halo-ZATAC#T0 did not degrade exogenous GFP-HaloTag protein in HEK293T cells (Supplementary Figs. 3b, c). Recognizing the critical role of linkers in targeted protein degradation, we synthesized a series of Halo-ZATACs with varying numbers of thymidine nucleotides as linkers, designated Halo-ZATAC#Tn. Notably, Halo-ZATAC#T3 and #T5 significantly enhanced GFP-HaloTag degradation (Fig. 2c, d). Live-cell fluorescence microscopy demonstrated that Halo-ZATAC#T3 treatment led to a reduction in GFP signal, which was preserved upon pretreatment with the proteasome inhibitor MG132 (Fig. 2e, f).

Further studies showed that Halo-ZATAC#T3 induced GFP-HaloTag degradation in a dose-dependent manner, with an estimated DC_{50} value of 44.15 nM (Fig. 2g, h). Time-course experiments indicated that degradation began at 6 h and persisted for up to 48 h (Fig. 2i, j). As expected, the Halo-ZATAC#T3-induced degradation was mediated by the $CRL2^{ZYG11B}$-dependent proteasomal pathway, confirmed by blockage of degradation with the proteasome inhibitor MG132, excessive Apt#Z6, and siRNAs targeting ZYG11B, but not by the lysosomal degradation inhibitor chloroquine (CQ) (Fig. 2k–p and Supplementary Fig. 3d, e). These results collectively confirm that Apt#Z6 is a highly suitable E3 ligase ligand for PROTAC discovery.

https://doi.org/10.1038/s41467-025-57823-5

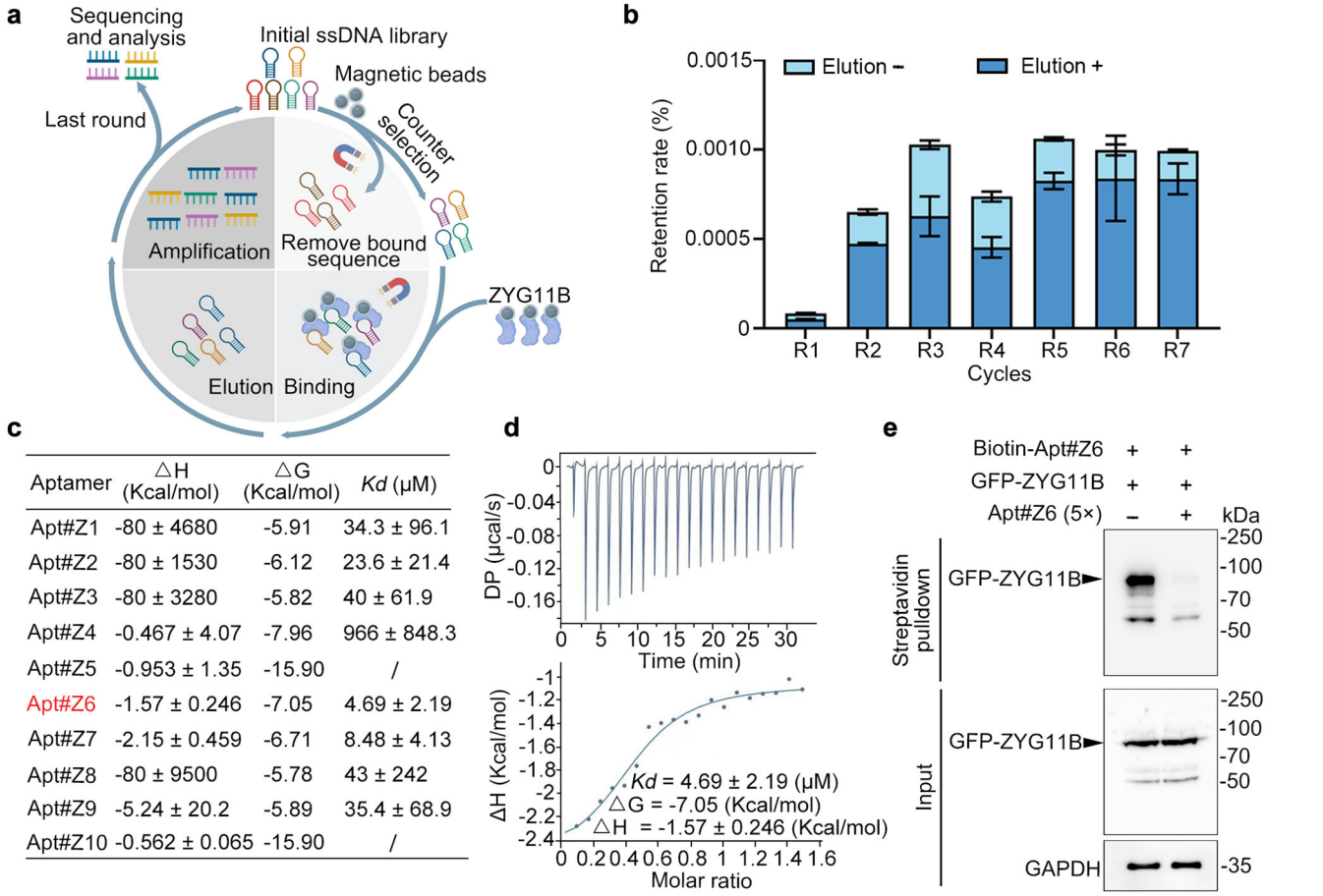

Aptamer	△H (Kcal/mol)	△G (Kcal/mol)	*Kd* (μM)
Apt#Z1	-80 ± 4680	-5.91	34.3 ± 96.1
Apt#Z2	-80 ± 1530	-6.12	23.6 ± 21.4
Apt#Z3	-80 ± 3280	-5.82	40 ± 61.9
Apt#Z4	-0.467 ± 4.07	-7.96	966 ± 848.3
Apt#Z5	-0.953 ± 1.35	-15.90	/
Apt#Z6	-1.57 ± 0.246	-7.05	4.69 ± 2.19
Apt#Z7	-2.15 ± 0.459	-6.71	8.48 ± 4.13
Apt#Z8	-80 ± 9500	-5.78	43 ± 242
Apt#Z9	-5.24 ± 20.2	-5.89	35.4 ± 68.9
Apt#Z10	-0.562 ± 0.065	-15.90	/

Fig. 1 | A non-inhibitory DNA aptamer targeting ZYG11B was identified. **a** Schematic of the SELEX procedure. Created with BioRender.com. **b** Positive and negative retention rates of the enriched DNA pool using RT-qPCR across rounds 1 to 7. **c**, **d** ITC was used to characterize the binding affinity of the aptamer candidates (**c**), with detailed ITC titration and fitting curves for Apt#Z6 shown (**d**). **e** Biotin-labeled Apt#Z6 was used to pull GFP-tagged ZYG11B down in HEK293T cells via a streptavidin pull-down assay, and the pellets were subjected to immunoblotting. The averages of $n = 2$ (B) and $n = 3$ (**c**, **d**) biologically independent samples are shown. Data are shown as the mean ± SD. The data presented in panel (**e**) are representative of three independent experiments.

Development of bispecific ZATACs for targeted degradation of oncogenic NCL

To further elucidate the practicability of Apt#Z6, we developed bispecific aptamer-based ZATACs, leveraging the facile self-assembly properties of aptamers. AS1411, a widely-used G-quadruplex aptamer that specifically targets the oncogenic NCL[27], was combined with Apt#Z6 to generate bispecific ZATACs, termed NCL-ZATACs (Fig. 3a). We tested three different types of linkers: initially, flexible double-stranded DNA linkers, where the flanking oligonucleotides were not complementarily paired, were assessed (Supplementary Fig. 4a). This configuration allowed good degradation efficiency with linkers equal to or longer than 18 base pairs (bp) (Supplementary Fig. 4b, c). However, the use of completely complementary double-stranded DNA linkers resulted in decreased degradation efficiency, requiring higher concentrations for effectiveness (Supplementary Fig. 4d–f). Similar outcomes were observed with single-stranded DNA linkers (Supplementary Fig. 4g–i). Consequently, we selected an NCL-ZATAC with a 20 bp flexible DNA linker, termed NCL-ZATAC#20, for further investigations.

To delve into the mechanism of NCL-ZATAC#20-mediated NCL degradation, we explored its ability to promote ternary complex formation. The binding affinity of NCL-ZATAC#20 for GFP-tagged NCL, forming a binary complex, was determined to be 668 nM, denoted as Kd^{binary} (Fig. 3b). Subsequently, NCL-ZATAC#20 was pre-incubated with ZYG11B protein, followed by incubation with GFP-NCL to form the ternary complex, denoted as $Kd^{ternary}$. Intriguingly, the $Kd^{ternary}$ value decreased to 259 nM, with a cooperativity factor (α) >1 (Fig. 3c), indicative of positive cooperativity within the ternary system[28,29]. Further, streptavidin pulldown and immunoprecipitation assays confirmed that NCL-ZATAC#20 interacted simultaneously with NCL and ZYG11B, substantiating the formation of the ternary complex (Fig. 3d, e).

NCL-ZATAC#20 degraded both exogenous and endogenous NCL in a dose-dependent manner, with estimated DC_{50} values of 166.6 nM and 158 nM, respectively, whereas the scrambled control (Scr-ZATAC#20), which features a scrambled sequence of Apt#Z6, had no effect on NCL degradation (Fig. 3f–h and Supplementary Fig. 5a, b). Time-course analysis indicated that NCL was rapidly degraded 4 h post-treatment with NCL-ZATAC#20 (Fig. 3i). In addition, NCL-ZATAC#20 remained stable in serum for 24 h (Supplementary Fig. 5c, d). Cycloheximide (CHX) chase assays revealed that NCL-ZATAC#20, other than Scr-ZATAC#20, significantly reduced the half-life of NCL (Fig. 3j, k). Fluorescence microscopy demonstrated that GFP-tagged NCL was substantially reduced by NCL-ZATAC#20 via proteasomal degradation (Fig. 3l). Further studies confirmed that NCL-ZATAC#20 induced NCL degradation through a ubiquitin-proteasome- and ZYG11B-dependent pathway, as evidenced by increased ubiquitination of NCL upon treatment with NCL-ZATAC#20 (Fig. 3m), and degradation was inhibited by the proteasome inhibitor MG132, excessive Apt#Z6, or siRNAs targeting ZYG11B, but not by the lysosomal degradation inhibitor CQ (Fig. 3n–p and Supplementary Fig. 5e).

https://doi.org/10.1038/s41467-025-57823-5

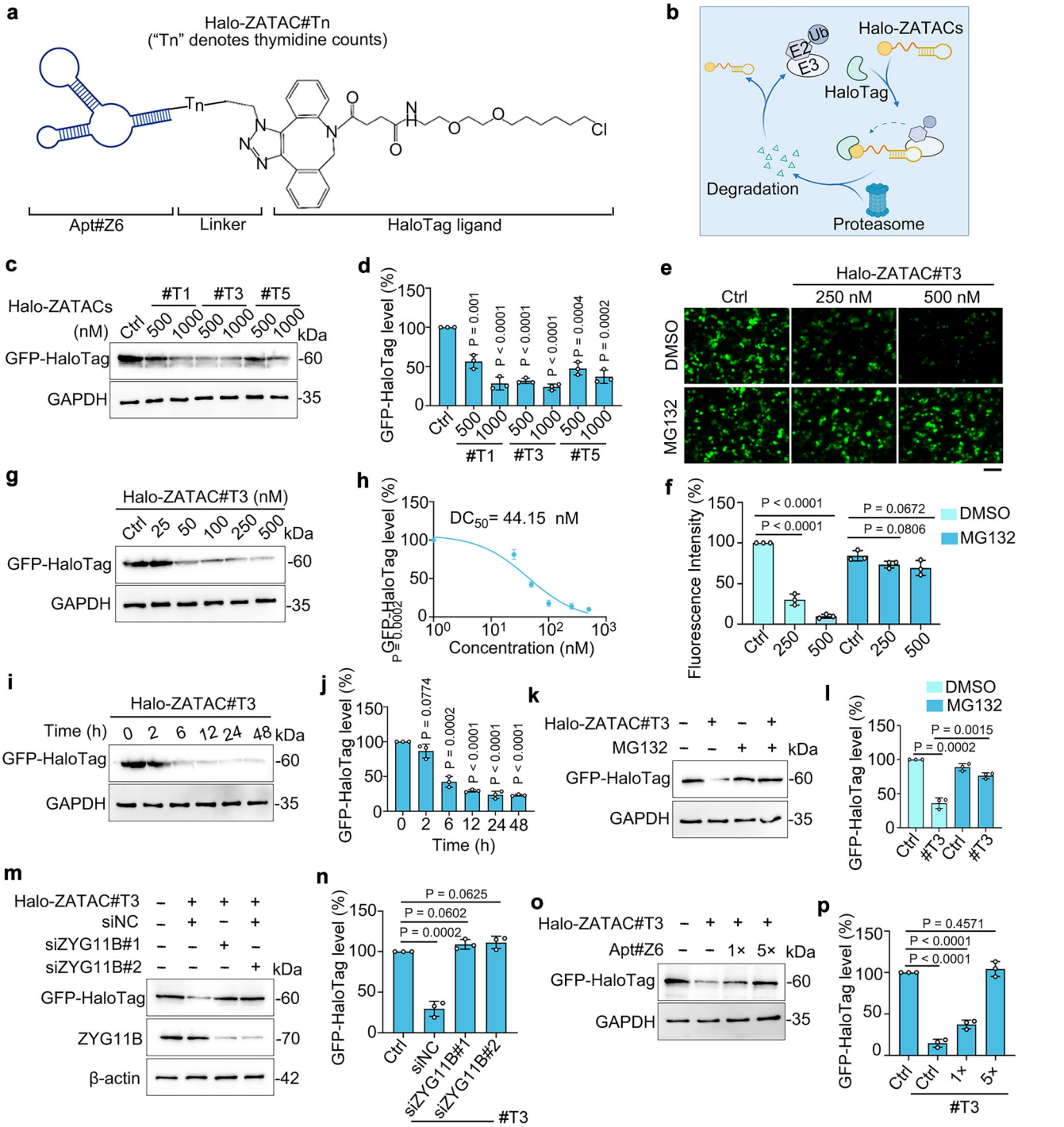

Fig. 2 | Construction of Halo-ZATACs to degrade GFP-HaloTag protein. **a** Structure of the Halo-ZATACs. "Tn", the number of thymidine nucleotides added to the 5′ end of Apt#Z6, serves as linkers. **b** Schematic of Halo-ZATAC-mediated degradation of GFP-HaloTag fusion protein through the ubiquitin-proteasome system. **c**, **d** GFP-HaloTag-expressing HEK293T cells were transfected with Halo-ZATAC#Tn for 24 h, and cell lysates were subjected to immunoblotting (**c**). The remaining GFP-HaloTag was quantified (**d**). #Tn ($n = 1, 3, 5$) represents Halo-ZATACs with one, three, or five thymine linkers. **e**, **f** Fluorescence imaging (**e**) and quantification (**f**) of GFP-HaloTag-expressing HEK293T cells treated with Halo-ZATAC#T3 in the presence or absence of MG132 (20 μM). Scale bar, 100 μm. **g**, **h** GFP-HaloTag-expressing HEK293T cells were transfected with escalating doses of Halo-ZATAC#T3 for 24 h and cell lysates were subjected to immunoblotting (**g**). The remaining GFP-HaloTag was quantified (**h**). **i**, **j** GFP-HaloTag-expressing HEK293T cells were transfected with Halo-ZATAC#T3 (500 nM) for the specified time points, and cell lysates were subjected to immunoblotting (**i**). The remaining GFP-HaloTag was quantified (**j**). **k**, **l** GFP-HaloTag-expressing HEK293T cells were transfected with Halo-ZATAC#T3 (500 nM) in the presence or absence of MG132 (20 μM) for 24 h, and cell lysates were subjected to immunoblotting (**k**). The remaining GFP-HaloTag was quantified (**l**). **m**, **n** GFP-HaloTag-expressing HEK293T cells were transfected with siRNAs targeting ZYG11B, followed by treating with Halo-ZATAC#T3 (500 nM) for 24 h. Cell lysates were subjected to immunoblotting (**m**), and the remaining GFP-HaloTag was quantified (**n**). **o**, **p** GFP-HaloTag-expressing HEK293T cells were transfected with Halo-ZATAC#T3 (500 nM) and Apt#Z6 for 24 h. Cell lysates were subjected to immunoblotting (**o**), and the remaining GFP-HaloTag was quantified (**p**). Figure 2a & b were created with BioRender.com. The averages of $n = 3$ (**d**, **h**, **f**, **j**, **l**, **n**, **p**) biological replicates are presented as mean ± SD. Statistical significance was determined using one-way ANOVA with multiple comparisons (**d**, **f**, **j**, **n**, **p**) and the *t* test (and nonparametric tests) in (**l**). The data presented in (**c**, **e**, **g**, **i**, **k**, **m**, **o**) are representative of three independent experiments.

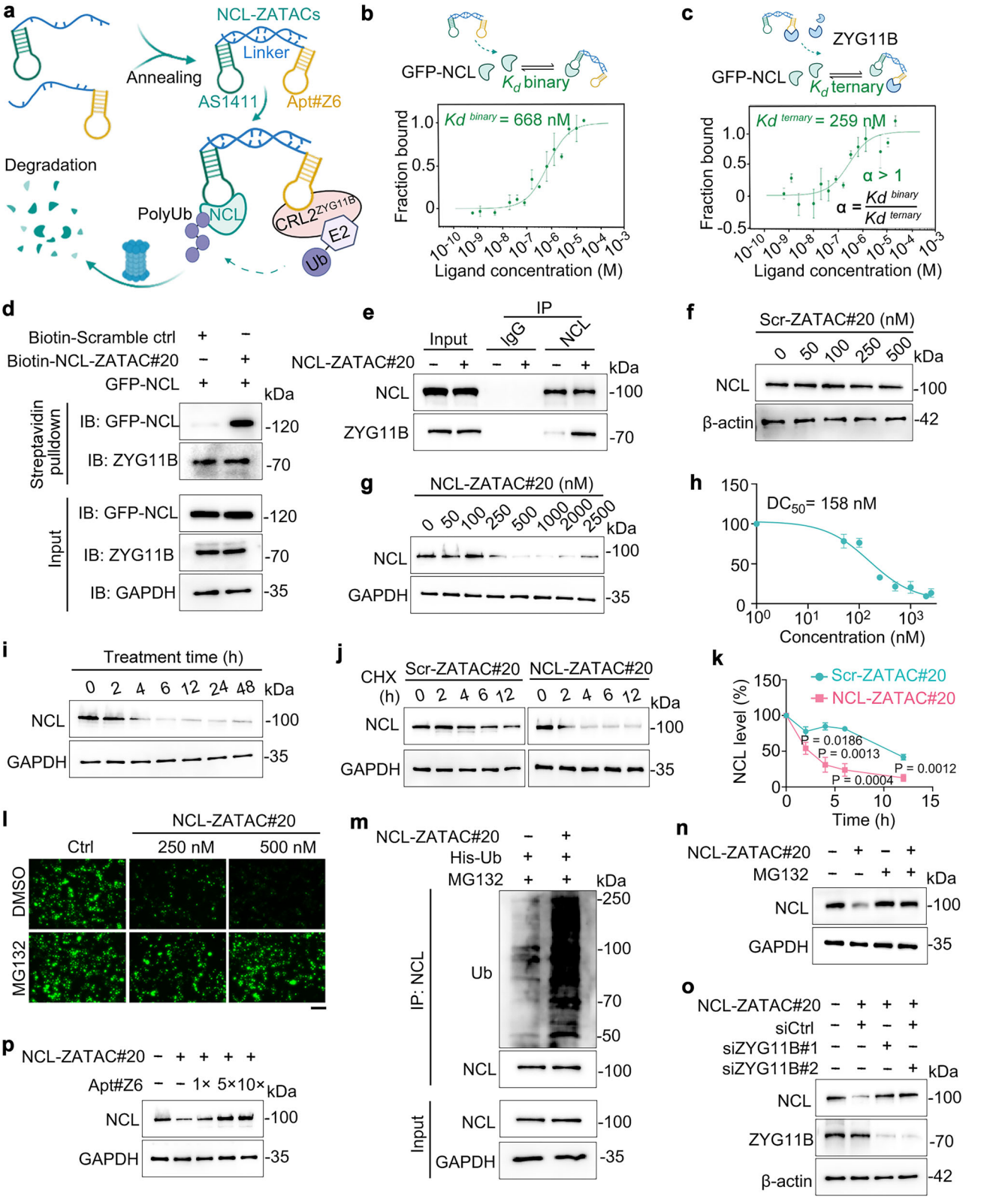

We next performed unbiased mass spectrometric experiments to ascertain the specificity of NCL-ZATAC#20, and found that over the 6000 proteins detected, 23 proteins, including GFP-NCL, were significantly degraded (Supplementary Fig. 5f). Further enrichment analysis by Metascape[30] revealed that the majority of downregulated proteins are involved in translation regulation, DNA metabolic process, and DNA transcription (Supplementary Fig. 5g). Given the critical role for NCL in ribosomal biogenesis, DNA metabolism, and gene transcription and translation[31], it is possible that the downregulation of these proteins stems from NCL degradation.

We next assessed the anti-tumor activity of NCL-ZATAC#20. Both the CCK-8 cell proliferation assay and colony formation assays demonstrated that NCL-ZATAC#20 significantly inhibited the growth of breast cancer cells, compared to PBS, AS1411, Apt#Z6, and Scr-

Fig. 3 | Bispecific aptamer-based ZATACs induce NCL degradation in a ZYG11B- and ubiquitin proteasome-dependent manner. a Schematic of NCL-ZATACs-mediated degradation of NCL. **b**, **c** Microscale thermophoresis (MST) to determine the binding affinity of GFP-NCL to NCL-ZATAC#20 (**b**) and to the NCL-ZATAC#20/ZYG11B complex (**c**). **d** Streptavidin pulldown assays to determine the interaction between NCL and ZYG11B proteins mediated by NCL-ZATAC#20 in GFP-NCL overexpressing HEK293T cells. For Biotin-Scramble ctrl, only NCL-targeted aptamer (AS1411) is scrambled, and the Apt#Z6 remains unchanged. **e** Co-immunoprecipitation assays to assess the interaction between endogenous NCL and ZYG11B in the presence or absence of NCL-ZATAC#20 (500 nM) in MG132-treated (20 μM) MCF-7 cells. **f**–**h** Immunoblotting analysis of MCF-7 cells treated with the specified concentrations of Scr-ZATAC#20 (**f**) or NCL-ZATAC#20 for 24 h (**g**). The remaining NCL was quantified (**h**). **i** Immunoblotting analysis of NCL levels in MCF-7 cells treated with NCL-ZATAC#20 (500 nM) for the specified time points. **j**, **k** Immunoblotting analysis of NCL levels in MCF-7 cells treated with NCL-ZATAC#20 and cycloheximide (CHX) for specified time points (**j**). The remaining NCL was quantified (**k**). **l** Fluorescence images of GFP-NCL-expressing HEK293T cells treated with NCL-ZATAC#20 in the presence or absence of MG132 (20 μM). Scale bar: 100 μm. **m** MCF-7 cells were transfected with His-Myc-Ub plasmids, followed by treating with NCL-ZATAC#20 and MG132 (20 μM) for 5 h. Cell lysates were subjected to immunoprecipitations. **n** Immunoblotting analysis of MCF-7 cells treated with NCL-ZATAC#20 (500 nM) in the presence or absence of MG132 (20 μM) for 24 h. **o** Immunoblotting analysis of MCF-7 cells transfected with ZYG11B-targeted siRNAs, followed by treating with NCL-ZATAC#20 (500 nM) for 24 h. **p** Immunoblotting analysis of MCF-7 cells treated with NCL-ZATAC#20 (500 nM) and varying concentrations of Apt#Z6. Figure 3a–c were created with BioRender.com. The averages of $n = 3$ (**b**, **c**, **h**, **k**) biologically independent samples are shown. Data are shown as the mean ± SD. Statistical significance in (**k**) was assessed using the t-tests (and nonparametric tests). The data shown in (**d**–**g**, **i**, **j**, **l**–**o**) are representative of three independent experiments.

ZATAC#20 control (Supplementary Fig. 6a–c). Furthermore, 3D tumor spheroid assays confirmed the antiproliferative effects of NCL-ZATAC#20 on breast cancer cells (Supplementary Fig. 6d, e). Collectively, these results highlight NCL-ZATAC#20 as a selective NCL degrader with potent antitumor activity.

Leveraging the bispecific ZATAC platform to degrade undruggable SOX2 and p53-R175H mutant

To verify the universality of the ZATAC platform, we selected the transcription factors SOX2 and the p53-R175H mutant as additional targets. Initially, we developed a series of bispecific SOX2-targeted ZATAC using a specific aptamer targeting SOX2[32], named SOX2-ZATACs (Fig. 4a). Immunoblotting results indicated that SOX2-ZATACs with a 20 bp linker (SOX2-ZATAC#20) demonstrated the highest degradation efficacy (Fig. 4b). Further studies showed that SOX2-ZATAC#20, unlike the scrambled control (Scr-ZATAC-2#20 in which Apt#6 is scrambled), degraded both exogenous and endogenous SOX2 in a dose-dependent manner (Fig. 4c and Supplementary Fig. 7a). Time-course experiments indicated that SOX2 protein degradation commenced at 6 h and persisted for 48 h (Fig. 4d). Co-immunoprecipitation assays revealed that SOX2-ZATAC#20 promoted the interaction between ZYG11B and SOX2, suggesting the formation of a ternary complex (Fig. 4e). As anticipated, SOX2-ZATAC#20 induced SOX2 degradation in a ubiquitin proteasome- and ZYG11B-dependent manner (Fig. 4f–i). We subsequently assessed the biological consequences of SOX2-ZATAC#20. EdU incorporation and CCK-8 cell proliferation assays demonstrated that SOX2-ZATAC#20 significantly inhibited the growth of lung cancer cells (Fig. 4j–l). The antiproliferative activity of SOX2-ZATAC#20 was further confirmed by colony formation and 3D tumor spheroid assays (Fig. 4m–p).

Next, we developed bispecific ZATACs targeting the p53 gain-of-function mutant, p53-R175H, using a selective p53-R175H-targeted aptamer (p53-mDA) developed in our previous study[33], hereafter termed R175H-ZATACs (Fig. 5a). For further studies, we utilized H1299 (p53 null) and H1299-p53-R175H stable cell lines (hereinafter referred to as H1299-R175H) (Supplementary Fig. 7b). We observed that the R175H-ZATAC with a 25 bp linker (R175H-ZATAC#25) exhibited the most effective degradation (Fig. 5b, c). R175H-ZATAC#25 degraded p53-R175H in a dose-dependent manner (Fig. 5d). Time-course experiments demonstrated that the degradation induced by R175H-ZATAC#25 commenced at 12 h and persisted for 48 h (Fig. 5e, f). Further investigations revealed that both MG132 and excess Apt#Z6 could inhibit the degradation of p53-R175H induced by R175H-ZATAC#25, indicating the critical involvement of ZYG11B and the ubiquitin proteasomal pathways (Fig. 5g, h and Supplementary Fig. 7c, d). Notably, treatment with R175H-ZATAC#25 inhibited the proliferation of H1299-R175H cells, presumably through the promoted degradation of p53-R175H (Fig. 5i–o). Taken together, these results confirm that the bispecific ZATAC is a general and versatile platform for targeted protein degradation.

Trispecific ZATACs enable efficient uptake and dual-target degradation

Leveraging aptamers or antibodies that recognize proteins overexpressed on the surface of cancer cells is a promising strategy for the development of aptamer- or antibody-drug conjugates[34]. Herein, we utilized the DNA three-way junction (3WJ), a Y-shaped configuration known for its exceptional plasticity and stability[35–37], as a framework for developing trispecific ZATACs, termed 3WJ-ZATACs (Fig. 6a). As a proof-of-concept, we employed AS1411, an aptamer specifically targeting NCL, which is overexpressed on the surface of many cancer cell types, as the delivery warhead to engineer 3WJ-ZATACs. Native PAGE analysis confirmed that the 3WJ-ZATAC was successfully assembled (Fig. 6b) and exhibited relatively good serum stability within 12 h (Supplementary Fig. 8a, b). Importantly, Cy3-labeled 3WJ-ScrApt#6, in which Apt#6 was replaced by a scrambled sequence, and Cy3-labeled 3WJ-ZATAC were effectively internalized into A549 cells (Fig. 6c). In contrast, Cy3-labeled 3WJ-Scr^{AS1411}, where AS1411 was replaced by a scrambled sequence, showed no internalization even at 12 h post-incubation (Fig. 6c and Supplementary Fig. 8c), underscoring the critical role of membrane-bound NCL in the uptake process.

Next, we generated a series of 3WJ-ZATACs with varied linkers and found that 3WJ-ZATAC#T10 was the most effective in degrading both SOX2 and NCL proteins (Supplementary Fig. 8d). 3WJ-ZATAC#T10 effectively degraded these proteins in A549 cells in both a dose- and time-dependent manner, whereas the negative control, 3WJ-Scr$^{Apt\#6}$, did not (Fig. 6d, e), highlighting the necessity of ZYG11B. Silencing the expression of NCL using siRNAs prevented 3WJ-ZATAC#T10-induced SOX2 degradation (Supplementary Fig. 8e). Live-cell images confirmed that Cy3-3WJ-ZATAC#T10 was successfully internalized into A549 cells, whereas NCL depletion alleviated the uptake (Supplementary Fig. 8f), implying the dependency of NCL for 3WJ-ZATAC#T10 uptake and subsequent degradation. In addition, live-cell images indicated that the majority of Cy3-3WJ-ZATAC did not colocalize with lysosomes, suggesting its capability to escape from the endosomal/lysosomal pathway (Supplementary Fig. 8g). As expected, MG132 treatment inhibited the 3WJ-ZATAC#T10-mediated degradation, suggesting the involvement of proteasomal pathways (Fig. 6f). Consequently, 3WJ-ZATAC#T10 significantly suppressed the growth of A549 cells, as demonstrated by colony formation and 3D tumor spheroid assays (Fig. 6g–j).

To establish the generality of the 3WJ-ZATAC platform, we replaced the aptamer AS1411 with Sgc8c, a specific aptamer for protein tyrosine kinase 7 (PTK7) that is overexpressed on the cell surface receptor of many cancers[38], and constructed 3WJ-ZATAC-PTK7. As

https://doi.org/10.1038/s41467-025-57823-5

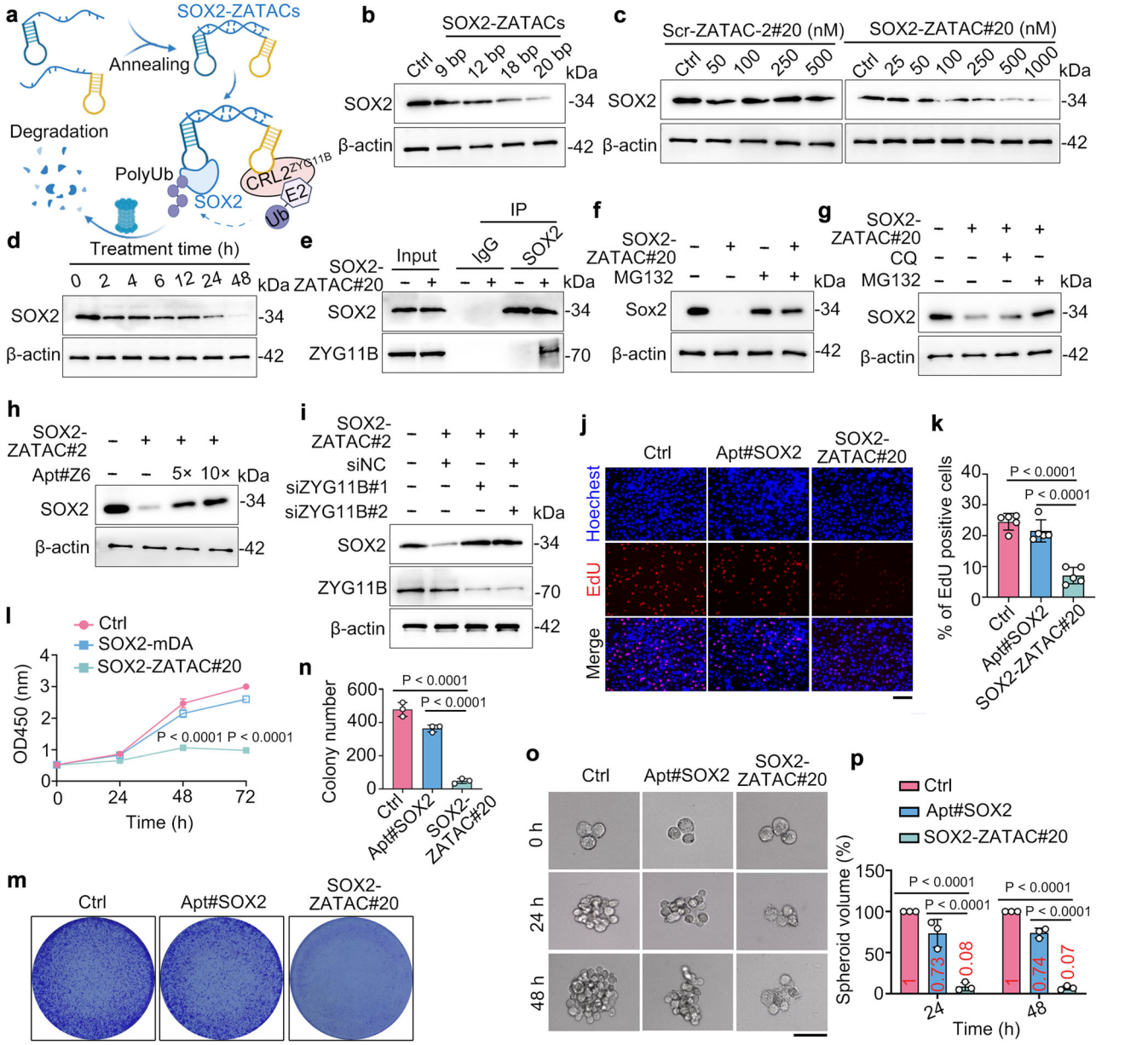

Fig. 4 | SOX2-ZATAC#20 efficiently degrades SOX2 and inhibits cancer cell proliferation. **a** Schematic of SOX2 degradation mediated by SOX2-ZATACs. Created with BioRender.com. **b** Immunoblotting analysis of A549 cells treated with SOX2-ZATACs with different lengths of double-stranded flexible linkers for 24 h. **c** Immunoblotting analysis of A549 cells treated with scramble control (Scr-ZATAC-2#20) or SOX2-ZATAC#20 for 24 h. **d** Immunoblotting analysis of A549 cells treated with SOX2-ZATAC#20 (500 nM) for the specified time points. **e** Co-immunoprecipitation assays to evaluate the interaction between endogenous SOX2 and ZYG11B in the presence or absence of SOX2-ZATAC#20 (500 nM) in MG132-treated (20 μM) A549 cells. **f**, **g** Immunoblotting analysis of A549 cells treated with SOX2-ZATAC#20 (500 nM), together with or without CQ (10 μM) or MG132 (20 μM) for 24 h. **h** Immunoblotting analysis of A549 cells treated with SOX2-ZATAC#20 (500 nM) and varying concentrations of Apt#Z6. **i** Immunoblotting analysis of A549 cells transfected with ZYG11B-targeted siRNAs, followed by treating with SOX2-ZATAC#20 (500 nM) for 24 h. **j**, **k** A549 cells were treated with PBS, Apt#SOX2 (500 nM), or SOX2-ZATAC#20 (500 nM) for 24 h, and were subjected to EdU incorporation assays (**j**). The percentage of EdU-positive cells was quantified (**k**). Scale bar: 100 μm. **l** A549 cells were treated with PBS, Apt#SOX2 (500 nM), or SOX2-ZATAC#20 (500 nM) for specified time points, and viable cells were evaluated using CCK-8 assays. **m**, **n** A549 cells were treated with PBS, Apt#SOX2 (500 nM), or SOX2-ZATAC#20 (500 nM) for two weeks and then subjected to crystal violet staining. The colonies were imaged (**m**) and quantified (**n**). **o**, **p** Representative 3D tumor spheroidic image (**o**) and quantification (**p**) of A549 cells treated with PBS, Apt#SOX2 (500 nM), or SOX2-ZATAC#20 (500 nM). Scale bar, 65 μm. The averages of $n = 5$ (k), $n = 4$ (l), $n = 3$ (**n**, **p**) biological replicates are shown. Data are shown as the mean ± SD. Statistical significance in (**k**, **l**, **n**, **p**) was assessed using one-way ANOVA with multiple comparisons. The data shown in (**b**–**j**, **m**, **o**) are representative of three independent experiments.

expected, both PTK7 and SOX2 were degraded by 3WJ-ZATAC-PTK7 (Fig. 6k). In addition, we generated another 3WJ-ZATAC, named 3WJ-ZATAC-p53, which co-degraded p53-R175H and NCL in H1299-R175H cells (Fig. 6l). These data collectively demonstrate that 3WJ-ZATACs are a promising platform for targeted delivery and protein degradation.

The tumor-specific distribution of 3WJ-ZATAC#T10 and its anti-tumor effect in vivo

To determine whether 3WJ-ZATAC#T10 could be efficiently delivered into tumor sites in vivo, we established tumor xenografts by subcutaneously transplanting A549 cells into BALB/c nude mice. Following this, Cy5-labeled 3WJ-ZATAC#T10 and control were injected into

https://doi.org/10.1038/s41467-025-57823-5

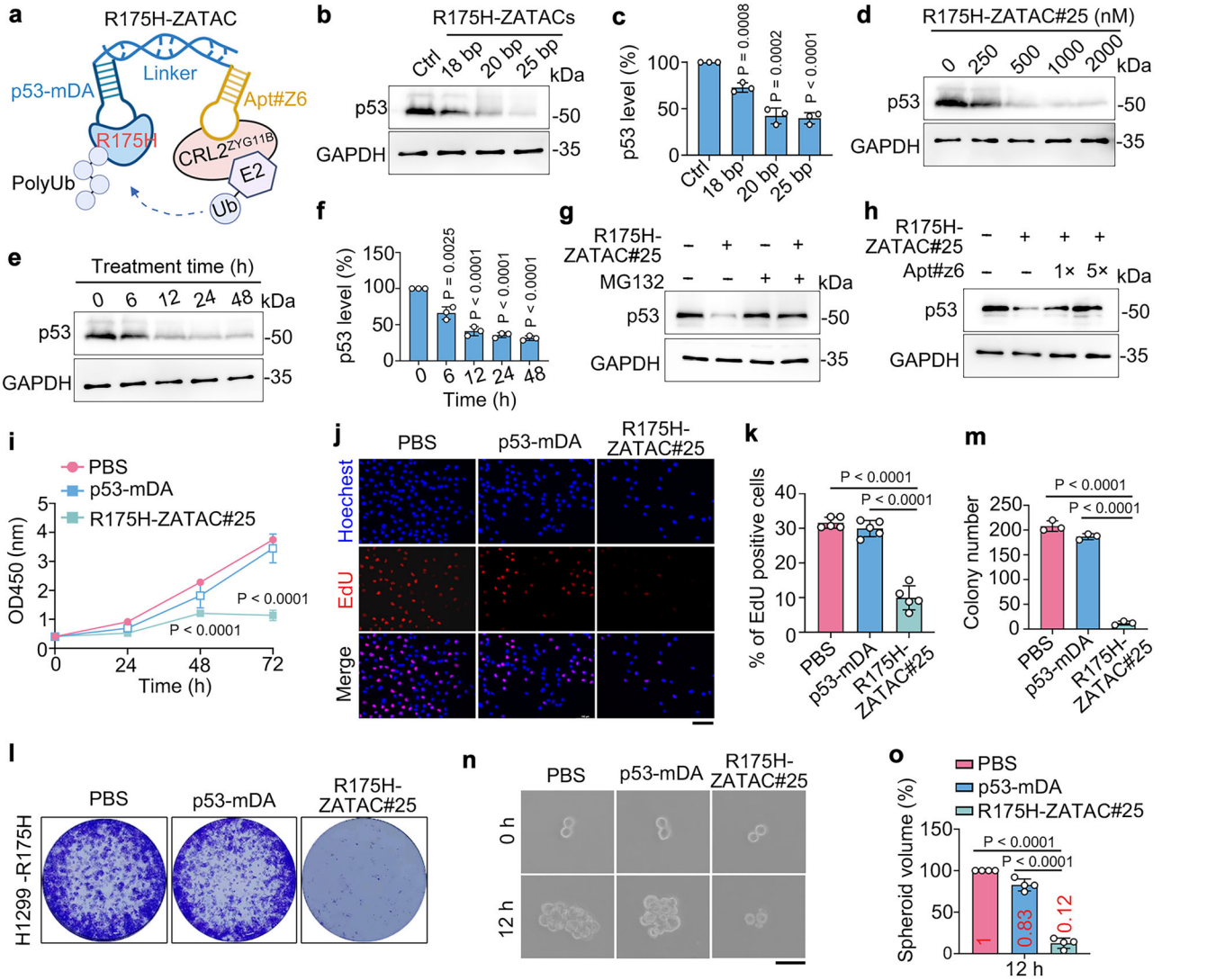

Fig. 5 | R175H-ZATAC#25 suppresses the growth of p53-R175H harboring cancer cells through degrading p53-R175H mutant. a Schematic of the degradation of p53-R175H induced by R175H-ZATACs. Created with BioRender.com. **b**, **c** Immunoblots (**b**) and quantification (**c**) of H1299-R175H cells treated with R175H-ZATACs (500 nM) for 24 h. **d** Immunoblotting analysis of H1299-R175H cells treated with R175H-ZATAC#25 for 24 h. **e**, **f** Immunoblotting analysis of H1299-R175H cells treated with R175H-ZATAC#25 (500 nM) for the indicated time points (**e**). The remaining p53-R175H was quantified (**f**). **g** Immunoblotting analysis of H1299-R175H cells treated with R175H-ZATAC#25 (500 nM) in the presence or absence of MG132 (20 μM) for 24 h. **h** Immunoblotting analysis of H1299-R175H cells treated with R175H-ZATAC#25 (500 nM) and Apt#Z6. **i** Cell proliferation assays to determine the effects of R175H-ZATAC#25 (500 nM) on H1299-R175H cells. **j**, **k** Fluorescence images (**j**) and quantification (**k**) of H1299-R175H cells treated with PBS, p53-mDA (500 nM), or R175H-ZATAC#25 (500 nM), followed by EdU staining. Scale bar, 100 μm. **l**, **m** H1299-R175H cells were treated with PBS, p53-mDA (500 nM), or R175H-ZATAC#25 (500 nM) for two weeks and then subjected to crystal violet staining. The colonies were imaged (**l**) and quantified (**m**). **n**, **o** Representative spheroidic images (**n**) and quantification (**o**) of H1299-R175H cells treated with PBS, p53-mDA (500 nM), or R175H-ZATAC#25 (500 nM). Scale bar, 65 μm. The averages of $n = 3$ (**c**, **f**, **m**), $n = 4$ (i, o), $n = 5$ (**k**) biological replicates are shown. Data are shown as the mean ± SD. Statistical significance in (**c**, **f**, **i**, **k**, **m**, **o**) was assessed using one-way ANOVA with multiple comparisons. The data shown in (**d**, **e**, **g**, **h**, **j**, **l**, **n**) are representative of three independent experiments.

the mice via the tail vein. As anticipated, a Cy5 fluorescence signal rapidly accumulated at the tumor sites post-injection, whereas no significant fluorescence signal was observed in the control-treated sites (Fig. 7a), indicating a tumor-specific distribution of 3WJ-ZATAC#T10 in vivo.

To further examine the anti-tumor activity of 3WJ-ZATAC#T10 in vivo, we randomly divided the xenografted mice into three groups and treated them bi-daily with PBS, 3WJ-Scr$^{Apt\#Z6}$, and 3WJ-ZATAC#T10 (Fig. 7b). Remarkably, 3WJ-ZATAC#T10 significantly suppressed tumor growth compared to both the PBS and 3WJ-Scr$^{Apt\#Z6}$ groups (Fig. 7c–e). Notably, no significant weight loss was observed in any of the groups (Fig. 7f). Histological examinations of the heart, liver, spleen, lung, and kidney sections revealed no noticeable toxicity attributable to 3WJ-ZATAC#T10 (Fig. 7g). Supporting these anti-tumor effects, immunohistochemical analyses confirmed that NCL and SOX2 were effectively degraded by 3WJ-ZATAC#T10 (Fig. 7h, i). Concurrently, the expression level of Ki67, a cell proliferation marker, decreased in the 3WJ-ZATAC#T10 treatment group. In contrast, levels of BCL2-associated X (BAX), an apoptotic marker, were elevated (Fig. 7h, i). Collectively, these results indicate that 3WJ-ZATAC#T10 is a potent dual-target degrader with tumor-targeting capabilities, suggesting its significant therapeutic potential for cancer treatment.

Discussion

Developing novel ligands for untapped E3 ligases is critical for targeted protein degradation[39]. Recently, Cao et al.[40] introduced a novel

https://doi.org/10.1038/s41467-025-57823-5

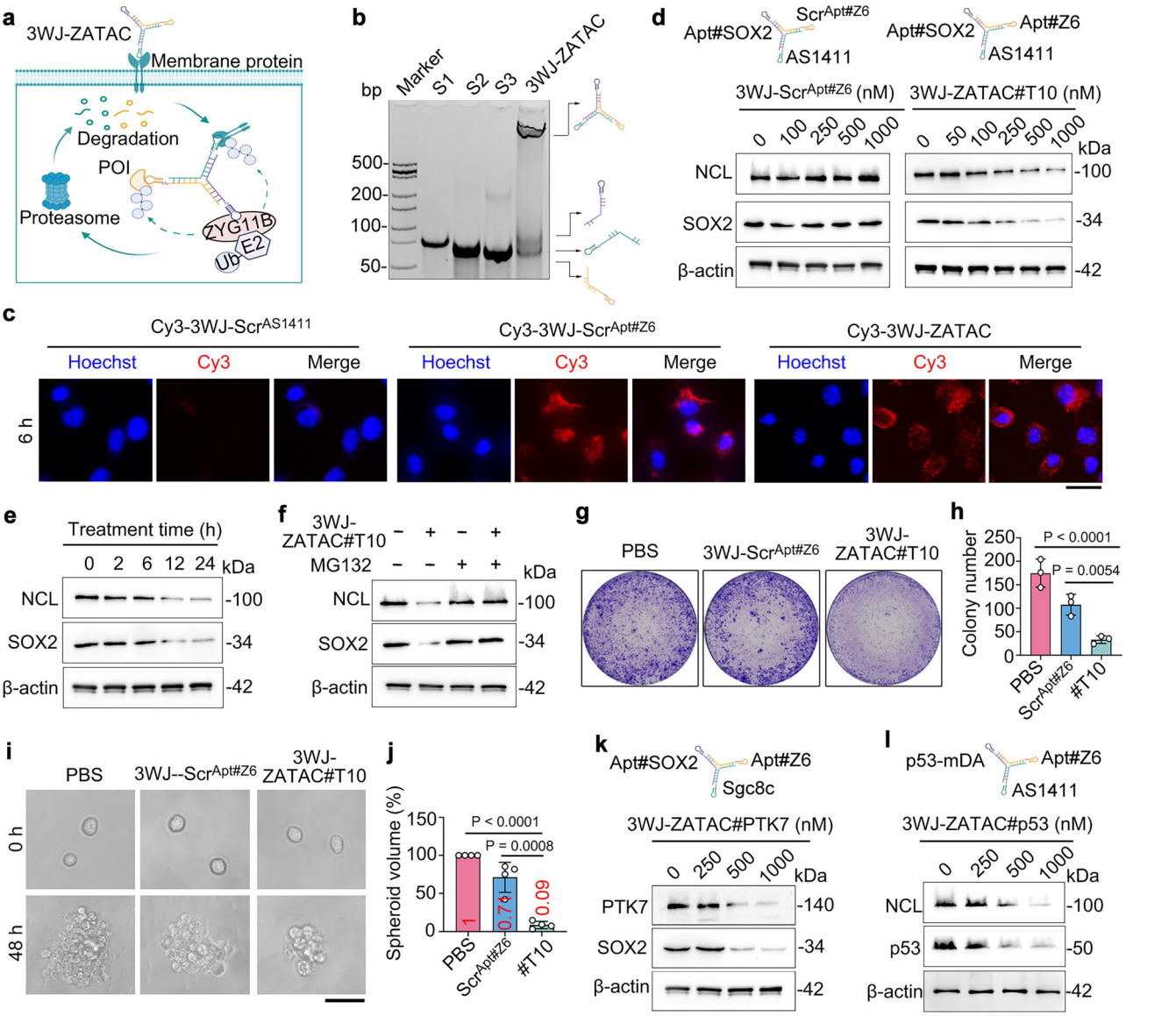

Fig. 6 | 3WJ-ZATACs enable targeted delivery and dual-target degradation. **a** Schematic depicting membrane protein-mediated 3WJ-ZATAC uptake and dual-target degradation. Created with BioRender.com. **b** Native PAGE showing the successful assembly of 3WJ-ZATAC. **c** Fluorescence images of A549 cells incubated with Cy3-3WJ-Scr^{AS1411} (1000 nM), Cy3-3WJ-Scr$^{Apt\#Z6}$ (1000 nM), or 3WJ-ZATAC (1000 nM) for 6 h. Scale bar, 20 μm. **d** Immunoblotting analysis of A549 cells treated with Cy3-3WJ-Scr$^{Apt\#Z6}$ or 3WJ-ZATAC#T10 for 24 h. **e** Immunoblotting analysis of A549 cells treated with 3WJ-ZATAC#T10 (1000 nM) for the specified time points. **f** Immunoblotting analysis of A549 cells treated with 3WJ-ZATAC#T10 (1000 nM) in the presence of MG132 (20 μM) for 24 h. **g**, **h** A549 cells were treated with PBS, 3WJ-Scr$^{Apt\#6}$ (1000 nM), or 3WJ-ZATAC#T10 (1000 nM) for two weeks and then subjected to crystal violet staining (**g**). The colonies were quantified (**h**). **i**, **j** Representative spheroidic images (**i**) and quantification (**j**) of A549 cells treated with PBS, 3WJ-Scr$^{Apt\#6}$ (1000 nM), or 3WJ-ZATAC#T10 (1000 nM). Scale bar, 65 μm. **k** Immunoblotting of A549 cells treated with 3WJ-ZATAC#PTK7 for 24 h. **l** Immunoblotting analysis of H1299-R175H cells treated with 3WJ-ZATAC#p53 for 24 h. The averages of $n = 3$ (**h**), $n = 4$ (**j**) biological replicates are shown. Data are shown as the mean ± SD. Statistical significance in (**h**, **j**) was assessed using one-way ANOVA with multiple comparisons. The data shown in (**b**–**g**, **i**, **k**, **l**) are representative of three independent experiments.

genetically expressing PROTAC platform, termed alncRNAs, which consists of an RNA aptamer targeting the protein of interest and partial sequences from HOTAIR, an artificial long non-coding RNA (lncRNA) specific for the E3 ligase Dzip3. The alncRNAs provide an effective, adaptable, and versatile strategy for targeted protein degradation. Although aptamers are promising molecular ligands, leveraging aptamers as E3 ligands for targeted protein degradation is not reported yet. To our knowledge, only one E3 ligase-targeted aptamer has been reported in the literature, which specifically recognizes the nuclear WW domain-containing E3 ubiquitin ligase 1 (WWP1)[41]. However, this aptamer is unsuitable for PROTAC discovery because it inhibits the ubiquitination activity of WWP1. In this study, we identified a DNA aptamer, Apt#Z6, that specifically targets ZYG11B without compromising the activity of the CRL2^{ZYG11B} ligase. We developed a modular and versatile Apt#Z6-based PROTAC platform, expanding the repertoire of E3 ligands and providing insights for employing aptamers to target other E3 ligases.

Although Apt#Z6 displays relatively low affinity to ZYG11B, the ZATACs are capable of robustly degrading the target proteins, probably because of the event-driven pharmacology and catalytic nature of PROTACs that enable the conversion of weak-affinity ligands into potent degraders. For instance, Prof. Crews and colleagues[42] developed an effective PROTAC for p38α ($DC_{50} = 210$ nM) using a ligand with weak affinity ($Kd = 11$ μM). This evidence together suggests that

https://doi.org/10.1038/s41467-025-57823-5

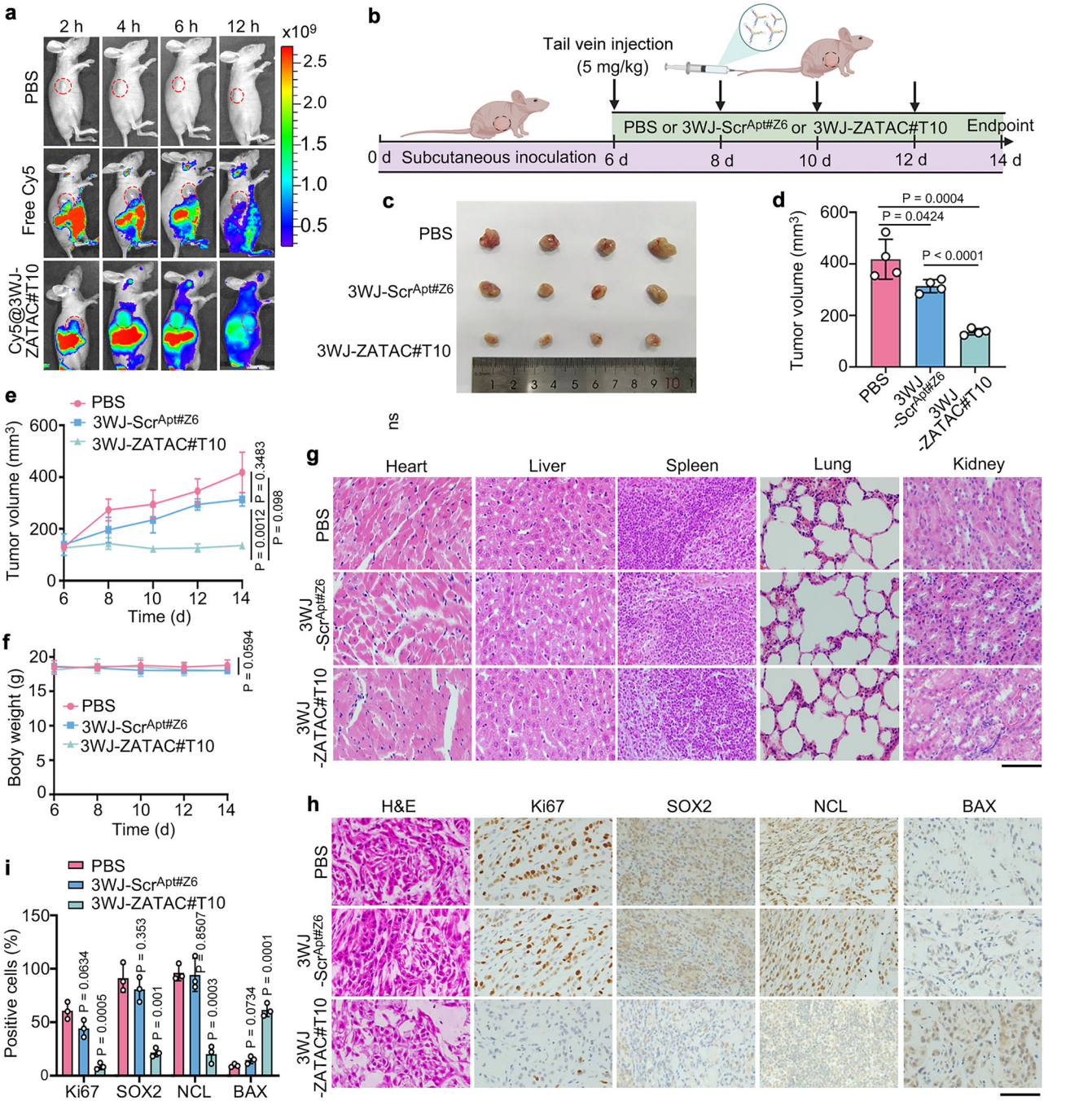

Fig. 7 | 3WJ-ZATAC#T10 inhibits tumor growth in vivo. a Images of xenograft mice injected with PBS, Cy5, or Cy5-3WJ-ZATAC#T10 via tail vein. **b** Schematic of the administration of tumor-bearing mice. Created with BioRender.com. **c**, **d** Images (**c**) and volumes (**d**) of tumors isolated from xenograft mice intravenously inoculated with PBS, 3WJ-Scr$^{Apt\#Z6}$ (5 mg/kg), or 3WJ-ZATAC (5 mg/kg). **e** Measurement of tumor volumes at specified times. **f** Measurement of body weight at the indicated intervals. **g** Histopathological examination of major organs post-treatment. Scale bar, 100 μm. **h**, **i** Immunohistochemistry images (**h**) and quantification (**i**) of tumor sections stained with the indicated antibodies. Scale bar, 100 μm. The averages of $n = 4$ (**d**–**f**) and $n = 3$ (**i**) biological replicates are shown. Data are shown as the mean ± SD. Statistical significance in (**d**–**f**, **i**) was assessed using one-way ANOVA with multiple comparisons. The data shown in (**g**, **h**) are representative of three independent experiments.

the low affinity between the PROTAC and the E3 ligase can be compensated by the interactions between the E3 ligase and target protein. Of course, it is warranted to identify aptamers with higher affinity to increase the efficiency of targeted protein degradation.

The length and types of linkers are critical for degradation efficacy[36]. Inspired by previous reports[43,44], we optimized the compositions of linkers in the bispecific aptamer-based ZATACs and identified flexible double-stranded DNA linkers as optimal. Further studies demonstrated that ZATACs with flexible double-stranded DNA linkers could effectively degrade SOX2 and p53-R175H proteins, supporting ZATACs as a general, modular, and straightforward platform. Importantly, transcription factors such as p53 and SOX2 are regarded as 'undruggable' targets. Aptamers, known as chemical antibodies, have shown great promise in targeting 'undruggable' proteins. In this context, using aptamers specifically targeting p53-R175H and SOX2, we successfully degraded these traditionally challenging targets using

ZATACs, reporting the first SOX2 degrader. Given the critical oncogenic role of SOX2 in various types of cancers[45–48], our SOX2-ZATAC may have therapeutic potential for cancer treatment.

Efficient and selective delivery of aptamer-based PROTACs into target tissues and cells poses significant challenges. Aptamers have been widely used for targeted delivery of therapeutic oligonucleotides into the cytoplasm of cancer cells through a unique mechanism that bypasses the endosomal/lysosomal pathway[49,50]. In this study, we utilized the 3WJ framework nucleic acids as a delivery system to address this issue. The 3WJ-ZATACs exhibit several advantageous properties, including uniform nanoscale dimensions, precise stoichiometry, high stability, and excellent biocompatibility[37]. By incorporating AS1411 or Sgc8c aptamer into the 3WJ-ZATACs, we achieved selective delivery and dual-target degradation. Furthermore, 3WJ-ZATACs demonstrated potent anti-tumor activity in vivo. Interestingly, the 3WJ-Scr$^{Apt\#Z6}$ also led to tumor regression to some extent, which may be attributed to the anti-tumor activities of the aptamer AS1411 present in the 3WJ-Scr$^{Apt\#Z6}$ [51].

Considering the efficacy of cell-SELEX in identifying aptamers that selectively recognize proteins prominently expressed on the surfaces of tumor cells[16], leveraging these aptamers to construct 3WJ-ZATACs offers substantial promise in mitigating off-tissue, on-target toxicity typically associated with potent PROTACs. In conclusion, our study provides compelling evidence of the universality and versatility of ZATACs and their therapeutic potential in cancer treatment, thus laying a solid foundation for advancing these degraders to clinical applications.

Methods

Materials

The pCDNA3-Myc-ubiquitin plasmid was acquired as outlined in previous studies[21]. Mammalian plasmids encoding GFP-HaloTAG, GFP-NCL, His-Ub, and Flag-SOX2 were obtained from the Public Protein/Plasmid Library (Nanjing, China). The following antibodies were employed: anti-NCL (Proteintech, #10556-1-AP), anti-SOX2 (Abways, #CY5268, for immunoblotting, and Proteintech, #11064-1-AP, for immunohistochemistry), anti-p53 (Proteintech, #60283-2-Ig), anti-ZYG11B (ImmunoWay, #YN4251), anti-His (Proteintech, #66005-1-Ig), anti-GFP (Abmart, #P30010), anti-GAPDH (Abcam, #ab8245), anti-Flag (ABclonal, #AE024), anti-RFP (Abclonal, #AE020), anti-Ki67 (Abways, #CY5542), anti-BAX (Abmart, #T40051), anti-JAK2 (Cell Signaling Technology, #3230), and anti-β-actin (Proteintech, #66009-1-Ig). The aptamers and their chemically modified versions (see Supplementary Data 1 and Supplementary MS analysis) were synthesized by the Beijing Genomics Institute (Beijing, China) and Sangon Biotech (Shanghai, China).

SELEX

The sequences of the DNA aptamer library (Aptamy Inc., Hefei, China) are as follows: 5′-TTCAGCACTCCACGCATAGC$(N)_{36}$CCTATGCGTG CTACCGTGAA-3′, where '$(N)_{36}$' signifies a sequence of 36 nucleotides composed of A, G, C, and T in equimolar proportions at each position. The SELEX process utilized magnetic beads for partitioning. The EDC/NHS protocol was employed to conjugate the purified ZYG11B protein onto magnetic beads. The DNA aptamer library was incubated with the ZYG11B protein in a PBS binding buffer for positive selection, and the magnetic beads were used for counter-selection (Supplementary Table 1). The aptamers that bound to ZYG11B were isolated and amplified via PCR. The first three rounds of amplification were conducted using conventional PCR, and the latter four rounds employed emulsion PCR (ePCR)[52]. Briefly, emulsion PCR oil (Aptamy Inc.) was added into the conventional PCR mix at a ratio of 1:4 (v/v) and the emulsion PCR was performed with the following conditions: preincubation at 95 °C for 3 min with 30 cycles of denaturation (1 min at 95 °C), annealing (1 min at 60 °C) and elongation (1 min at 72 °C), followed by a final extension at 72 °C for 5 min. The emulsion was then disrupted by the addition of isobutanol. The long-short chain method was used to generate a single-stranded DNA (ssDNA) pool for subsequent rounds of SELEX. After seven rounds of selection, the enriched DNA pool underwent high-throughput sequencing, followed by the analysis of the sequencing data using RazerS to map the enriched library reads[53].

Protein purification

ZYG11B and Zyg-11 homolog B-like protein (ZYG11BL or known as ZER1) proteins were purified as described previously[10]. The genes encoding human ZYG11B segments (amino acid residues 445-728) and ZER1 (amino acid residues 520–766) were cloned into the pET28-MKH8SUMO vector (Addgene, #79526). The proteins were expressed in *E. coli* strain BL21 (DE3) and purified using Ni-NTA beads at 4 °C. Briefly, non-specifically bound proteins were washed away with a buffer containing 20 mM Tris-HCl (pH 7.5), 400 mM NaCl, and 25 mM imidazole. The His-SUMO-ZYG11B and His-SUMO-ZER1 fusion proteins were then eluted using a buffer consisting of 20 mM Tris-HCl (pH 7.5), 400 mM NaCl, and 500 mM imidazole (pH 7.5). The purified proteins were dialyzed overnight at 4 °C in the presence of TEV protease to cleave the His-SUMO tag. Subsequently, it was passed through a Ni-NTA column (GE Healthcare, Pittsburgh, USA) to remove the cleaved His-SUMO tag and TEV protease. Further purification was achieved using a HiTrap Q HP column and a Superdex 200 Increase 10/300 GL column (GE Healthcare) in a buffer containing 20 mM Tris-HCl (pH 7.5), 150 mM NaCl, and 1 mM DTT. The final purified protein was concentrated and stored at − 80 °C.

ITC

ITC experiments were conducted at 16 °C using the MicroCal PEAQ-ITC system (Malvern Panalytical, Worcestershire, UK). The ZYG11B or ZER1 protein was prepared in an ITC buffer comprising 150 mM NaCl and 20 mM Tris-HCl at pH 7.5. Concentrations were adjusted to 50–70 μM for the ZYG11B or ZER1 protein and 0.5–1.4 mM for the aptamers. Each aptamer injection was set at 1.5 μL, except for the initial injection of 0.5 μL. Injections were spaced by a 150 s interval, with a reference power setting of 10 μcal/sec. The binding stoichiometry (N), dissociation constant (*Kd*), and thermodynamic parameters, including changes in enthalpy (ΔH), entropy (ΔS), and Gibbs free energy (ΔG), were determined using a single-site binding model with MicroCal PEAQ-ITC analysis software version 1.30.

Synthesis of Halo-ZATACs, bispecific ZATACs, and trispecific ZATACs

Halo-ZATACs were synthesized by coupling a dibenzocyclooctyne (DBCO)-modified HaloTAG ligand (see Supplementary Methods) with an azide-functionalized Apt#Z6 via a click chemistry reaction at 37 °C for 2.5 h, followed by purification using a 3 K ultrafiltration membrane (Millipore, Burlington, MA) to remove excess DBCO-HaloTAG ligand. For the construction of bispecific or trispecific ZATACs, individual aptamers were first denatured at 95 °C in PBS buffer and rapidly cooled on ice. Subsequently, the pairing aptamers were mixed and incubated at 4 °C for 30 min to facilitate self-assembly. Native polyacrylamide gels were used to visualize the assembled ZATACs.

MST

To determine the binding affinity of ZYG11B to Apt#Z6, purified ZYG11B protein was serially diluted and mixed with Cy5-labelled Apt#Z6. To assess the affinity of NCL-ZATACs to NCL, NCL-ZATAC#20 was serially diluted and mixed with GFP-tagged NCL protein. For the ternary complex, NCL-ZATAC#20 was diluted in MST buffer, pre-incubated with ZYG11B protein, and subsequently mixed with GFP-tagged NCL protein using previously described methods[54]. After a 15 min incubation, the mixtures were loaded into hydrophobic capillaries of a Monolith NT™ system and analyzed using a Monolith NT.115

instrument (NanoTemper Technologies, Munich, Germany). The *Kd* values were determined using MO affinity analysis software provided by NanoTemper Technologies.

SPR

SPR experiments were conducted at a controlled temperature of 25 °C using the Biacore T200 system (GE Healthcare). Biotinylated Apt#Z6 was covalently attached to a Series S SA chip. ZYG11B protein was prepared in SPR running buffer containing 20 mM Tris, 250 mM NaCl, 0.2% (w/v) PEG 3350, 0.2% (w/v) BSA, 1 mM TCEP, 0.05% TWEEN 20, and 1% DMSO at pH 7.5. This setup allowed for evaluating the Apt#Z6-ZYG11B interaction over a concentration range of 0.003 μM to 100 μM. Data were analyzed using Biacore T200 evaluation software version 2.0, with sensorgrams corrected for reference and blank signals. Blank injections utilized the running buffer, with bulk effects meticulously adjusted through solvent correction.

GPS assays

Stable GPS reporter cells were generated as previously described[12]. The stability of the N-degron-GFP fusion protein was assessed by measuring the GFP/RFP ratio using an ACEA NovoCyte flow cytometer (ACEA Biosciences, Inc.), with RFP serving as the internal control. Data analysis was performed using FlowJo software.

Cell culture and transfection

MCF-7, A549, H1299, and HEK293T cells were sourced from the American Type Culture Collection. The H1299-R175H stable cells (a kind gift from Prof. Ge Shan) were generated as described[55]. All the cell lines used in this study have been authenticated by STR profiling. These cells were maintained in DMEM or 1640 medium, supplemented with 10% fetal bovine serum (FBS) and 1% penicillin/streptomycin, and incubated at 37 °C in a 5% CO_2 atmosphere. Halo-ZATACs, bispecific ZATACs (NCL-ZATACs, SOX2-ZATACs, and R175H-ZATACs), and various plasmids were transfected into cells using Lipofectamine 3000 (Thermo Fisher Scientific), following the manufacturer's protocols. 3WJ-ZATACs were added directly into the culture medium without any assistance of transfection reagents. siRNAs targeting ZYG11B and NCL (RiboBio, Guangzhou, China) were transfected using Lipofectamine RNAiMAX (MilliporeSigma, Burlington, MA, USA). For cycloheximide chase (CHX) assays, MCF-7 cells were treated with CHX (10 μg/mL) alone or in combination with Scr-ZATAC#20 (500 nM) or NCL-ZATAC#20 (500 nM) for specified time points.

Immunoblotting

Proteins were resolved by 10% sodium dodecyl sulfate-polyacrylamide gel electrophoresis (SDS-PAGE), transferred to PVDF membranes, and probed with primary antibodies followed by HRP-conjugated goat anti-rabbit and anti-mouse secondary antibodies (Abways, Shanghai, China) at room temperature (see Supplementary Data 2 for antibody information). The target proteins were visualized using an enhanced chemiluminescence substrate kit (MilliporeSigma).

Co-immunoprecipitation and streptavidin pulldown assays

Cells were lysed using ice-cold cell lysis buffer (250 mM NaCl, 0.5% Triton X-100, 10% glycerol, 1 mM DTT, 1 mM PMSF, 50 mM Tris-HCl, pH 7.4) supplemented with a protease inhibitor cocktail. For co-immunoprecipitation assays, antibodies against NCL, SOX2, and ZYG11B were added to cell lysate supernatants and incubated overnight at 4 °C. Subsequently, the antibody-protein complexes were incubated with protein A/G-agarose beads (#P2055, Beyotime) for 4 h. The immunoprecipitated proteins were subjected to immunoblotting. For streptavidin pulldown assays, cell lysates were treated with biotinylated Apt#Z6 or ZATACs overnight at 4 °C, followed by incubation for 4 h with streptavidin-agarose beads (MilliporeSigma) at 4 °C. The bound complexes were subjected to immunoblotting.

Serum stability assays

The Apt#Z6 and ZATACs were incubated in a complete culture medium supplemented with 10% FBS at 37 °C for specified time points. DNA samples were analyzed using 15–20% native PAGE, stained with GelRed, and visualized using a ChemiDoc Imaging System with UV illumination (Bio-Rad, Hercules, CA, USA).

Cell proliferation assays

For CCK-8 cell proliferation assays, cells were seeded in 96-well plates and treated with control, aptamers, or ZATACs for designated durations. Cell viability was determined using a CCK-8 kit (MedChemExpress, Shanghai, China). For colony formation assays, cells (500 per well) were plated in 12-well plates and transfected with control aptamers, or ZATACs. After two to three weeks, cells were fixed with 4% paraformaldehyde and stained with 0.4% crystal violet. Colonies were imaged, and the number of colonies was quantified. For EdU incorporation assays, cells on coverslips were treated with control, aptamers, or ZATACs, followed by incubation with an EdU kit (RiboBio, Guangzhou, China) for 4 h. Cells were then fixed with 4% paraformaldehyde for 15 min, permeabilized with 0.5% Triton X-100 for 10 min, stained with Apollo staining solution for 30 mins, and counterstained with Hoechst for 30 min. Coverslips were mounted on slides and imaged with a TCS SP8 confocal microscope (Leica, Solms, Germany).

3D cell culture

3D cell culture assays were conducted as previously described[21]. Briefly, cells were seeded into ultra-low attachment surface 12-well plates. After a two-day incubation period, the spheroids were treated with control aptamers, or ZATACs for the specified duration. Spheroids were imaged using an inverted microscope, and their volumes were measured using ImageJ software in a double-blind manner.

Animal experiments

BALB/c mice were purchased from Beijing Vital River Laboratory Animal Technology (Beijing, China) and housed at 22 °C under specific-pathogen-free conditions and controlled humidity (60% ± 10%) with a standard 12 h light/dark cycle. All animal experiments were conducted in accordance with protocols approved by the Institutional Animal Care and Use Committee of Tianjin Medical University General Hospital (IRB2024-DW-113). A549 cells in 50% Matrigel were subcutaneously injected into the flank of 5-week-old female BALB/c mice. Once tumors reached a volume of 100–150 mm^3, the mice were randomly divided into three groups and administered intravenously with PBS, 3WJ-$Scr^{Apt\#Z6}$ (5 mg/kg), or 3WJ-ZATAC#T10 (5 mg/kg) via tail vein injection every other day. Tumor dimensions—length (L) and width (W)—were measured at specified time points, and tumor volume was calculated using the formula $V = (L \times W^2) / 2$. At the endpoint, mice were euthanized, and major organs and tumors were harvested for further analysis.

For in vivo imaging, mice bearing A549 tumors were randomly divided into three groups and administered with PBS, free Cy5 (5 mg/kg), or Cy5@3WJ-ZATAC#T10 (5 mg/kg) via tail vein injections. The mice were anesthetized and imaged at intervals of 2, 4, 6, and 12 h post-injection using a Syngene PXi imaging system (Synoptics Technologies Ltd., Cambridgeshire, UK).

Immunohistochemistry staining

The heart, liver, spleen, lung, and kidney tissues were fixed in 4% neutral-buffered paraformaldehyde for 24 h, stained with hematoxylin and eosin (H&E), and examined under a light microscope for histopathological analysis in a double-blind manner. Formalin-fixed, paraffin-embedded samples from xenograft tumors were subjected to immunohistochemistry staining with the indicated antibodies. The samples were probed with primary antibodies and subsequently with

HRP-conjugated anti-mouse and anti-rabbit secondary antibodies (Servicebio, Wuhan, China), followed by staining with 3–3′-diaminobenzidine (DAB) chromogen (Servicebio), counterstained with hematoxylin, and cover-slipped for visualization under a TCS SP8 confocal microscope (Leica).

Statistical analysis

The statistical methods and the sample sizes are indicated in the figure legends. Statistical analysis was performed using GraphPad Prism v8.0 (GraphPad Software, La Jolla, CA, USA). Data were analyzed using Student's *t* test for pairwise comparisons and analysis of variance (ANOVA) for multiple group comparisons, with significance thresholds set at a *P*-value < 0.05.

Reporting summary

Further information on research design is available in the Nature Portfolio Reporting Summary linked to this article.

Data availability

All data are included in the main text and Supplementary Information or available from the authors. The raw numbers for charts and graphs are available in the Source Data file whenever possible. The aptamer sequencing data have been deposited in NCBI under the accession code PRJNA1220334. The mass spectrometry proteomics data have been deposited in the ProteomeXchange Consortium via the PRIDE partner repository under the code of PXD060634. Source data are provided in this paper.

References

1. Schapira, M., Calabrese, M. F., Bullock, A. N. & Crews, C. M. Targeted protein degradation: expanding the toolbox. *Nat. Rev. Drug Discov.* **18**, 949–963 (2019).
2. Zhao, L., Zhao, J., Zhong, K., Tong, A. & Jia, D. Targeted protein degradation: mechanisms, strategies and application. *Signal Transduct. Target. Ther.* **7**, 113 (2022).
3. Burslem, G. M. & Crews, C. M. Proteolysis-targeting chimeras as therapeutics and Tools for biological discovery. *Cell* **181**, 102–114 (2020).
4. Li, Y., Song, J., Zhou, P., Zhou, J. & Xie, S. Targeting undruggable transcription factors with PROTACs: advances and perspectives. *J. Med. Chem.* **65**, 10183–10194 (2022).
5. Békés, M., Langley, D. R. & Crews, C. M. PROTAC targeted protein degraders: the past is prologue. *Nat. Revs. Drug Discov.* **21**, 181–200 (2022).
6. Buckley, D. L. et al. Targeting the von Hippel-Lindau E3 ubiquitin ligase using small molecules to disrupt the VHL/HIF-1α interaction. *J. Am. Chem. Soc.* **134**, 4465–4468 (2012).
7. Jan, M., Sperling, A. S. & Ebert, B. L. Cancer therapies based on targeted protein degradation - lessons learned with lenalidomide. *Nat. Rev. Clin. Oncol.* **18**, 401–417 (2021).
8. Jevtic, P., Haakonsen, D. L. & Rape, M. An E3 ligase guide to the galaxy of small-molecule-induced protein degradation. *Cell Chem. Biol.* **28**, 1000–1013 (2021).
9. Mahrour, N. et al. Characterization of Cullin-box sequences that direct recruitment of Cul2-Rbx1 and Cul5-Rbx2 modules to Elongin BC-based ubiquitin ligases. *J. Biol. Chem.* **283**, 8005–8013 (2008).
10. Yan, X. et al. Molecular basis for recognition of Gly/N-degrons by CRL2(ZYG11B) and CRL2(ZER1). *Mol. Cell* **81**, 3262–3274 (2021).
11. Timms, R. T. et al. A glycine-specific N-degron pathway mediates the quality control of protein N-myristoylation. *Science* **365**, eaaw4912 (2019).
12. Li, Y. et al. CRL2(ZER1/ZYG11B) recognizes small N-terminal residues for degradation. *Nat. Commun* **13**, 7636 (2022).
13. Mena, E. L. et al. ORF10-Cullin-2-ZYG11B complex is not required for SARS-CoV-2 infection. *Proc. Natl. Acad. Sci. USA* **118**, e2023157118 (2021).
14. Zhang, J. et al. ZYG11B potentiates the antiviral innate immune response by enhancing cGAS-DNA binding and condensation. *Cell Rep.* **42**, 112278 (2023).
15. Duan, B. et al. LncRNA LINC01871 sponging miR-142-3p to modulate ZYG11B promotes the chemoresistance of colorectal cancer cells by inducing autophagy. *Anti Cancer Drug* **34**, 827–836 (2023).
16. Zhou, J. & Rossi, J. Aptamers as targeted therapeutics: current potential and challenges. *Nat. Rev. Drug Discov.* **16**, 181–202 (2017).
17. Zhu, G. & Chen, X. Aptamer-based targeted therapy. *Adv. Drug Deliv. Rev* **134**, 65–78 (2018).
18. Yang, Z., Pang, Q., Zhou, J., Xuan, C. & Xie, S. Leveraging aptamers for targeted protein degradation. *Trends Pharmacol. Sci.* **44**, 776–785 (2023).
19. He, S. et al. Aptamer-PROTAC Conjugates (APCs) for tumor-specific targeting in breast cancer. *Angew. Chem. Int. Ed. Engl* **60**, 23299–23305 (2021).
20. Kong, L. et al. Selective degradation of the p53-R175H oncogenic hotspot mutant by an RNA aptamer-based PROTAC. *Clin. Transl. Med.* **13**, e1191 (2023).
21. Chen, M. et al. Inducible degradation of oncogenic nucleolin using an aptamer-based PROTAC. *J. Med. Chem.* **66**, 1339–1348 (2023).
22. Wang, Y. et al. Antitumor effect of anti-c-Myc aptamer-based PROTAC for degradation of the c-Myc protein. *Adv. Sci.* **11**, e2309639 (2024).
23. Wu, Y. et al. Aptamer-LYTACs for targeted degradation of extracellular and membrane proteins. *Angew. Chem. Int. Ed. Engl.* **62**, e202218106 (2023).
24. Li, Y. et al. Covalent LYTAC enabled by DNA aptamers for immune checkpoint degradation therapy. *J. Am. Chem. Soc.* **145**, 24506–24521 (2023). 45.
25. Ody, B. K. et al. Synthesis and evaluation of cereblon-recruiting HaloPROTACs. *Chembiochem* **24**, e202300498 (2023).
26. Buckley, D. L. et al. HaloPROTACS: Use of small molecule PROTACs to induce degradation of HaloTag fusion proteins. *ACS Chem. Biol.* **10**, 1831–1837 (2015).
27. Carvalho, J., Mergny, J. L., Salgado, G. F., Queiroz, J. A. & Cruz, C. G-quadruplex, friend or foe: the role of the G-quartet in anticancer strategies. *Trends Mol. Med.* **26**, 848–861 (2020).
28. Gadd, M. S. et al. Structural basis of PROTAC cooperative recognition for selective protein degradation. *Nat. Chem. Biol.* **13**, 514–521 (2017).
29. Roy, M. J. et al. SPR-measured dissociation kinetics of PROTAC ternary complexes influence target degradation rate. *ACS Chem. Biol.* **14**, 361–368 (2019).
30. Zhou, Y. et al. Metascape provides a biologist-oriented resource for the analysis of systems-level datasets. *Nat. Commun.* **10**, 1523 (2019).
31. Mongelard, F. & Bouvet, P. Nucleolin: a multiFACeTed protein. *Trends Cell Biol.* **17**, 80–86 (2007).
32. Liu, K. et al. Targeting SOX2 protein with peptide aptamers for therapeutic gains against esophageal squamous cell carcinoma. *Mol. Ther.* **28**, 901–913 (2020).
33. Kong, L. et al. An engineered DNA aptamer-based PROTAC for precise therapy of p53-R175H hotspot mutant-driven cancer. *Sci. Bull.* **69**, 2122–2135 (2024).
34. Santos, T. et al. Recognition of nucleolin through interaction with RNA G-quadruplex. *Biochem. Pharmacol.* **189**, 114208 (2021).
35. Sabir, T. et al. Branchpoint expansion in a fully complementary three-way DNA junction. *J. Am. Chem. Soc.* **134**, 6280–6285 (2012).
36. Taghdisi, S. M., Danesh, N. M., Ramezani, M., Yazdian-Robati, R. & Abnous, K. A novel AS1411 aptamer-based three-way junction

pocket DNA nanostructure loaded with doxorubicin for targeting cancer cells in vitro and in vivo. *Mol. Pharm.* **15**, 1972–1978 (2018).
37. Shu, D., Shu, Y., Haque, F., Abdelmawla, S. & Guo, P. Thermodynamically stable RNA three-way junction for constructing multifunctional nanoparticles for delivery of therapeutics. *Nat. Nanotechnol.* **6**, 658–667 (2011).
38. Liu, M. et al. Aptamer-targeted DNA nanostructures with doxorubicin to treat protein tyrosine kinase 7-positive tumours. *Cell Prolif.* **52**, e12511 (2019).
39. Hanzl, A. & Winter, G. E. Targeted protein degradation: current and future challenges. *Curr. Opin. Chem. Biol.* **56**, 35–41 (2020).
40. Cao, C. et al. Engineering artificial non-coding RNAs for targeted protein degradation. *Nat. Chem. Biol.* https://doi.org/10.1038/s41589-024-01719-w (2024).
41. Tucker, W. O., Kinghorn, A. B., Fraser, L. A., Cheung, Y. W. & Tanner, J. A. Selection and characterization of a DNA aptamer specifically targeting human HECT ubiquitin ligase WWP1. *Int. J. Mol. Sci.* **19**, 763 (2018).
42. Bondeson, D. P. et al. Lessons in PROTAC design from selective degradation with a promiscuous warhead. *Cell Chem. Biol.* **25**, 78–87 (2018).
43. Wang, L. et al. Bispecific Aptamer induced artificial protein-pairing: a strategy for selective inhibition of receptor function. *J. Am. Chem. Soc.* **141**, 12673–12681 (2019).
44. Zhu, Y. & Hart, G. W. Dual-specificity RNA aptamers enable manipulation of target-specific O-GlcNAcylation and unveil functions of O-GlcNAc on β-catenin. *Cell* **186**, 428–445 (2023).
45. Mahlokozera, T. et al. Competitive binding of E3 ligases TRIM26 and WWP2 controls SOX2 in glioblastoma. *Nat. Commun.* **12**, 6321 (2021).
46. Grimm, D. et al. The role of SOX family members in solid tumours and metastasis. *Semin. Cancer Biol.* **67**, 122–153 (2020).
47. Novak, D. et al. SOX2 in development and cancer biology. *Semin. Cancer Biol.* **67**, 74–82 (2020).
48. Kasashima, H. et al. Stromal SOX2 upregulation promotes tumorigenesis through the generation of a SFRP1/2-expressing cancer-associated fibroblast population. *Dev. Cell* **56**, 95–110 (2021).
49. Wan, L. Y. et al. An exploration of aptamer internalization mechanisms and their applications in drug delivery. *Expert Opin. Drug Deliv.* **16**, 207–218 (2019).
50. Kotula, J. W. et al. Aptamer-mediated delivery of splice-switching oligonucleotides to the nuclei of cancer cells. *Nucleic Acid Ther.* **22**, 187–195 (2012).
51. Girvan, A. C. et al. AGRO100 inhibits activation of nuclear factor-kappaB (NF-kappaB) by forming a complex with NF-kappaB essential modulator (NEMO) and nucleolin. *Mol. Cancer Ther.* **5**, 1790–1799 (2006).
52. Yufa, R. et al. Emulsion PCR significantly improves nonequilibrium capillary electrophoresis of equilibrium mixtures-based aptamer selection: allowing for efficient and rapid selection of aptamer to unmodified ABH2 protein. *Anal. Chem.* **87**, 1411–1419 (2015).
53. Weese, D., Emde, A. K., Rausch, T., Döring, A. & Reinert, K. RazerS–fast read mapping with sensitivity control. *Genome Res.* **19**, 1646–1654 (2009).
54. Bartoschik, T., Zoephel, A., Rumpel, K., Ciulli, A. & Heffern, C. MST and TRIC technology to reliably study PROTAC binary and ternary binding in drug development. *Methods Mol. Biol.* **2365**, 115–133 (2021).
55. Chen, L. et al. The isolation of an RNA aptamer targeting to p53 protein with single amino acid mutation. *Proc. Natl. Acad. Sci. USA* **112**, 10002–10007 (2015).

Acknowledgements

We thank Dr. Ge Shan from the University of Science and Technology of China for the H1299-R175H stable cells. This work was supported by grants from the National Natural Science Foundation of China (32270892, 32070708 to S.X., and 32200613 to M.C., and 32100656 to X.D., and 82321001 to C.D.), Shandong Provincial Natural Science Foundation (ZR2021MC157 to M.C.), and Tianjin Key Medical Discipline (Specialty) Construction project (TJYXZDXK-028A to X.D.).

Author contributions

C.H.X., C.D., H.Y., and S.X. supervised the project and designed the experiments. Z.Y., M.C., R.G., P.Z., W.P., J.S., S.M., S.C., C.Y.X., M.Z., H.C., H.N., X.Y., and X.D. performed the experiments. Z.Y., M.C., H.C., W.M., J.Z., and S.X. analyzed data. Z.Y. and S.X. wrote the manuscript.

Competing interests

The authors declare no competing interests.

Additional information

Supplementary information The online version contains supplementary material available at https://doi.org/10.1038/s41467-025-57823-5.

Correspondence and requests for materials should be addressed to Chenghao Xuan, Cheng Dong, Hua Yan or Songbo Xie.

Peer review information *Nature Communications* thanks Da Han, Patrick Potts, Satpal Virdee, and the other anonymous reviewer(s) for their contribution to the peer review of this work. A peer review file is available

[1]Key Laboratory of Breast Cancer Prevention and Therapy (Ministry of Education); Key Laboratory of Immune Microenvironment and Disease (Ministry of Education); The Province and Ministry Co-sponsored Collaborative Innovation Center for Medical Epigenetics, Department of Biochemistry and Molecular Biology, Tianjin Medical University; Department of Ophthalmology, Tianjin Medical University General Hospital, Tianjin, China. [2]School of Life Sciences and

Medicine, Shandong University of Technology, Zibo, China. [3]Center for Cell Structure and Function, Collaborative Innovation Center of Cell Biology in Universities of Shandong, College of Life Sciences, Shandong Normal University, Jinan, China. [4]Department of Ophthalmology, Ministry of Education International Joint Laboratory of Ocular Diseases, Tianjin Key Laboratory of Ocular Trauma, Tianjin Institute of Eye Health and Eye Diseases, China-UK "Belt and Road" Ophthalmology Joint Laboratory, Tianjin Medical University General Hospital, Tianjin, China. [5]School of Medicine, Nankai University, Tianjin, China. [6]School of Basic Medical Sciences, Tianjin Medical University, Tianjin, China. [7]State Key Laboratory of Medicinal Chemical Biology, Tianjin Key Laboratory of Protein Science, Haihe Laboratory of Cell Ecosystem, College of Life Sciences, Nankai University, Tianjin, China. [8]Department of Medicinal Chemistry, Tianjin Key Laboratory on Technologies Enabling Development of Clinical Therapeutics and Diagnostics, School of Pharmacy, Tianjin Medical University, Tianjin, China. [9]Tianjin Key Laboratory of Spine and Spinal Cord, Department of Orthopaedics, Tianjin Medical University General Hospital, Tianjin, China. [10]Department of Hematology, Tianjin Key Laboratory of Bone Marrow Failure and Malignant Hemopoietic Clone Control, Tianjin Institute of Hematology, Tianjin Medical University General Hospital, Tianjin, China. [11]These authors contributed equally: Zhihao Yang, Miao Chen.
✉e-mail: chenghaoxuan@tmu.edu.cn; dongcheng@tmu.edu.cn; zyyyanhua@tmu.edu.cn; songboxie@tmu.edu.cn